

## Porous plates at incidence

Chandan Bose,\* Callum Bruce, and Ignazio Maria Viola†

*School of Engineering, Institute for Energy Systems, University of Edinburgh, Edinburgh, EH9 3FB, UK*

This paper investigates the effect of permeability on two-dimensional rectangular plates at incidences. The flow topology is investigated for Reynolds number ( $Re$ ) values between 30 and 90, and the forces on the plate are discussed for  $Re = 30$ , where the wake is found to be steady for any value of the Darcy number ( $Da$ ) and the flow incidence ( $\alpha$ ). At  $Re = 30$ , for a plate normal to the stream and vanishing  $Da$ , the wake shows a vortex dipole with a stagnation point on the plate surface. With increasing  $Da$ , the separation between the vortex dipole and the plate increases; the vortex dipole shortens and is eventually annihilated at a critical  $Da$ . For any value of  $Da$  below the critical one, the vortex dipole disappears with decreasing  $\alpha$ . However, at low  $Da$ , the two saddle-node pairs merge at the same  $\alpha$ , annihilating the dipole; while at high  $Da$ , they merge at different  $\alpha$ , resulting in a single recirculating region for intermediate incidences. The magnitudes of lift, drag, and torque decrease with  $Da$ . Nevertheless, there exists a range of  $Da$  and  $\alpha$ , where the magnitude of the plate-wise force component increases with  $Da$ , driven by the shear on the plate's pressure side. Finally, the analysis of the fluid impulse suggests that the lift and drag reduction with  $Da$  are associated with the weakening of the leading and trailing edge shear layer, respectively. The present findings will be directly beneficial in understanding the role of permeability on small porous wings.

### I. INTRODUCTION

The flow around porous bodies has a wide range of applications, including aerospace [1, 2] and environmental [3, 4] engineering, and offshore energy [5]. Most of these applications are concerned with high Reynolds number ( $Re$ ) flows, where the wake of the permeable body is turbulent. However, some biological flyers such as plant seeds [6], and applications such as bio-inspired microflyers for environmental monitoring [7], are concerned with low Reynolds number flows, for which the effect of permeability is yet to be fully understood. To this end, this paper considers the effect of permeability for the canonical flow past a two-dimensional (2D) rectangular plate immersed in a uniform and constant flow stream.

The flow past 2D *impervious* plates has been extensively studied experimentally [8–13], numerically [9, 10, 14–19], as well as theoretically [20]. When the plate is orthogonal to the stream, i.e. at an incidence  $\alpha = 90^\circ$ , flow separation occurs at the edges of the plate [20]. For Reynolds number ( $Re$ ) values below a critical threshold, which decreases with the width-to-thickness ratio ( $\chi$ ), a steady vortex dipole is formed in the wake of the plate [21]. The critical  $Re$  decreases, for example, from 115 to 30 for  $\chi = 1/4$  and 10, respectively [20, 22]. The vortex dipole is attached to the plate with its upstream stagnation point on the plate surface. The downstream, stagnation point shifts downstream with increasing  $Re$ , resulting in a greater vortex dipole, and vortex shedding occurs for  $Re$  higher than the critical threshold [16]. The wake remains 2D up to a critical  $Re$  that also decreases with  $\chi$ . For example, the critical  $Re$  at which the wake turns three-dimensional is 165 and 95 for  $\chi = 0.006$  and 4, respectively [16, 21].

How the flow topology varies with  $\alpha$  is known for an *impervious* plate. At  $\alpha = 0$ , the plate is aligned with the flow but separation occurs due to the blunt leading edge if  $\chi > 0$ . For  $\chi$  greater than a threshold that depends on  $Re$ , the flow reattaches forming a leading edge bubble [23, 24], and the flow remains attached up to the downstream blunt trailing edge. If  $Re$  is sufficiently low to ensure a steady wake, increasing  $\alpha$ , the flow topology changes from attached flow to a single vortex, and eventually to a vortex dipole as  $\alpha$  approaches  $90^\circ$  [15].

The effect of permeability has been investigated for porous squared cylinders [25–28], circular cylinders [29], aerofoils [30], spheres [31, 32], and axisymmetric disks [27, 33–35]. These studies reveal that the flow past permeable bodies is governed by  $Re$ , the Darcy number  $Da$ , and the porosity  $\epsilon$  [36, 37]. However,  $\epsilon$  only weakly affects the flow field and its stability [27]. In general, in the wake of permeable bluff bodies, a steady recirculation region exists for low  $Re$  and low  $Da$ ; vortex shedding occurs for high  $Re$  and low  $Da$ ; while the wake is steady without recirculation for high  $Da$ . The  $Re$  and  $Da$  thresholds depend on the geometry [27, 35]. For example, for a permeable disk orthogonal to the flow and with  $\chi = 10$ , the maximum  $Da$  at which a recirculation region exists is  $10^{-3}$  with a mild non-monotonic dependency on  $Re$  [33, 35].

Two-dimensional permeable plates have only been investigated at high  $Re$  and at  $\alpha = 90^\circ$ , i.e. where a vortex dipole exists only in the time average sense for low  $Da$  [38–40]. Instead, the effect of permeability on 2D plates at low  $Re$  and various  $\alpha$  has not been investigated before. To that end, in this paper, we numerically study the flow past 2D porous plates with  $\chi = 10$  and porosity  $\epsilon = 0.95$ , for a range of  $Da$ , and  $\alpha$  values. We first study the steady-to-unsteady wake transition for a range of  $Re$

\* now at Aerospace Engineering, School of Metallurgy and Materials, The University of Birmingham, Birmingham, B15 2TT, United Kingdom

† i.m.viola@ed.ac.uk

values, and then carry out a detailed flow-field and force analysis at  $Re = 30$ , where the wake remains steady throughout the chosen parametric space.

The remainder of the paper is structured as follows. The numerical method, including detailed domain size and grid resolution independent study and solver validation, is presented in §II. The results and discussions are presented in §III. These include, first, the identification of the transition from a steady to an unsteady wake in the  $Re - Da$  parameter space (§III A); then the analysis of the flow-field past a plate normal to the stream (§III B) and at different incidences with the stream (§III C); finally, the analysis of how the forces and torque change with  $\alpha$  and  $Da$  (§III D) and the identification, using impulse theory, of the associated changes in the vorticity field (§III E). The salient outcomes of this study are summarised in §IV.

## II. METHODOLOGY

We model a 2D porous plate with width  $\hat{d}$  and thickness  $\hat{f}$  in a uniform stream of fluid with density  $\hat{\rho}$  and velocity  $\hat{u}_\infty$ . The hat over the symbols is used to indicate dimensional quantities. In the following, all quantities are made nondimensional using the base  $(\hat{\rho}, \hat{d}, \hat{u}_\infty)$ . We define two different frames of reference (Fig. 1a): (1) a global frame of reference  $O(X, Y)$ , where  $X$  and  $Y$  are parallel and orthogonal to  $\hat{u}_\infty$ , respectively; and (2) a body fixed frame of reference  $O(x, y)$ , where  $x$  and  $y$  are in the plate-normal and plate-wise direction, respectively. The angle of attack  $\alpha$  is defined as the complementary angle to the angle between the two frames of references, and thus  $O(X, Y) = O(x, y)$  when  $\alpha = 90^\circ$ . Figure 1b schematically presents the separated vortex dipole in the wake of a porous plate normal to the stream, where the saddle points and nodes are marked by  $S1, S2$ , and  $N1, N2$ , respectively.

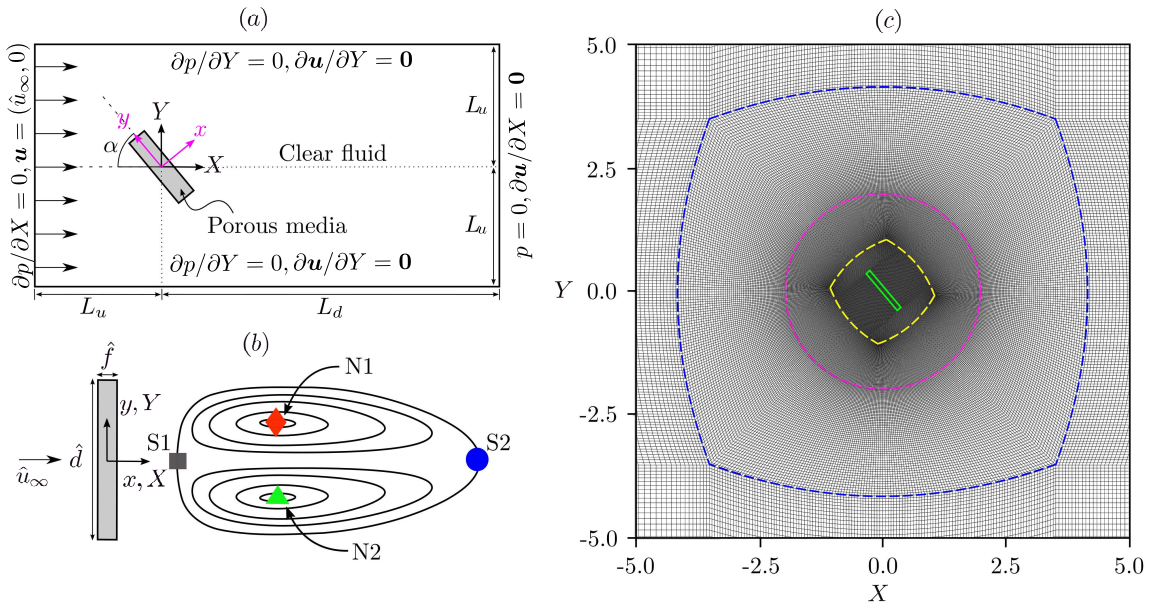


FIG. 1: (a) Computational domain and boundary conditions (not to scale). (b) Schematic of the vortex dipole in the wake of a porous plate normal to the stream; saddle points  $S1, S2$ , and nodes  $N1, N2$  are labelled. (c) Computational grid near the porous plate (green) at  $\alpha = 50^\circ$ . The external H-type grid transforms to O-type on the blue dashed line, and back to H-type on the yellow dashed line. The magenta dashed line is the interface about which the internal part of the grid is rotated for varying  $\alpha$ .

### A. Governing equations and numerical approach

We solve, in the  $O(X, Y)$  frame, the continuity equation and the Darcy-Brinkman-Forchheimer equation [36, 37, 41], which are, in nondimensional form,

$$\nabla \cdot \mathbf{u} = 0, \quad (1)$$

$$\frac{1}{\epsilon} \frac{\partial \mathbf{u}}{\partial t} + \frac{1}{\epsilon^2} (\mathbf{u} \cdot \nabla) \mathbf{u} = -\nabla p + \frac{1}{\epsilon Re} \nabla^2 \mathbf{u} - \frac{1}{Re Da} \mathbf{u} - \frac{c_F}{\sqrt{Da}} |\mathbf{u}| \mathbf{u}, \quad (2)$$

where  $\mathbf{u} = (u, v)$  is the nondimensional velocity vector with components  $u$  and  $v$ ;  $t$  is the nondimensional time;  $p$  is the nondimensional pressure; and  $c_F$  is a form-drag coefficient.

In this study, we consider  $\epsilon = 0.95$  and  $c_F = 0$ , but different values are adopted to validate our results with those of other authors (see Sec. II D). We have developed a customised porous incompressible Navier-Stokes solver, `porousIcoFoam`, by modifying the `icoFoam` solver, available within the finite volume method based open-source library `OpenFOAM`. The spatial and temporal discretisations are second-order accurate. The Pressure Implicit with the Splitting of the Operator algorithm with a predictor step and two pressure correction loops has been used to couple the pressure and velocity equations. A preconditioned conjugate gradient iterative solver is used to solve the pressure equation, whereas a diagonal incomplete-Cholesky method is used for preconditioning. A preconditioned smooth solver is used to solve the pressure-velocity coupling equation, and the symmetric Gauss-Seidel method is used for preconditioning. The absolute error tolerance criteria for pressure and velocity are set to  $10^{-6}$ . The simulations are run for 240 convective periods ( $0 \leq t \leq 240$ ). This ensures convergence of the steady-state loads with relative errors smaller than  $10^{-8}$ .

## B. Computational domain

The porous plate is placed within a rectangular computational domain with the edges parallel to the  $X$  and  $Y$  axes. The plate is placed at a distance  $L_u = 20$  from the upstream and the lateral sides of the domain and  $L_d = 80$  from the downstream edge (Fig. 1a). At the upstream edge (inlet), we set  $\mathbf{u} = (u_\infty, 0)$  and  $\partial p / \partial X = 0$ , while at the downstream edge (outlet),  $p = 0$  and  $\partial \mathbf{u} / \partial X = \mathbf{0}$ . On the side edges, we apply a slip condition with  $\partial p / \partial Y = 0$  and  $\partial \mathbf{u} / \partial Y = \mathbf{0}$ .

Equation 2 is solved both inside and outside of the porous plate. In the clear fluid region, outside of the plate,  $\epsilon = 1$  and  $Da \rightarrow \infty$ , and thus eq. 2 simplifies into the incompressible Navier-Stokes equation for Newtonian fluids. At the edges of the plate, which is the interface between the clean fluid and the porous media, velocity, pressure, and stresses are conserved.

The domain is made of an external region, which is fixed for all simulations, and an internal region, which is rotated by  $\alpha$ . The grid topology is shown in Fig. 1c. The initial condition is a uniform flow on the whole domain with  $\mathbf{u} = (u_\infty, 0)$  and  $p = 0$ .

## C. Forces calculations

The fluid forces generated by the plate are computed from the pressure and shear forces acting on the edges of the plate, i.e. at the interface between the clean fluid and the porous media. Once the steady state is reached, the force is

$$\mathbf{F} = \oint_L p \mathbf{n} \, dl + \oint_L \mathbf{S} \cdot \mathbf{n} \, dl, \quad (3)$$

where  $\mathbf{n}$  is the unit vector locally normal to the plate perimeter  $l$  and pointing outwards;  $\mathbf{S}$  is the viscous stress tensor. It is noted that using the base  $(\hat{\rho}, \hat{d}, \hat{u}_\infty)$ , the force and torque coefficients are twice the nondimensional forces and torque. The lift, drag, and torque coefficients are  $C_L = 2L$ ,  $C_D = 2D$ , and  $C_M = 2M$ , respectively. The torque is computed with respect to the origin of the frames and is positive anticlockwise.

## D. Verification and validation

To estimate the modelling error due to the finite dimension of the domain, and the numerical error due to the finite cell size, we consider three cases and compare the results with those of other authors. Case 1 is a steady simulation of the flow past a rectangular cylinder (i.e.  $\chi = 1$ ) with  $Re = 30$ ,  $Da = 10^{-3}$ ,  $\epsilon = 0.977$ , and  $c_F = 0.148$ . This case was modelled by Dhinakaran and Ponmozhi [25] and by Anirudh and Dhinakaran [26]. Case 2 is an unsteady simulation of the same geometry ( $\chi = 1$ ) with  $Re = 75$ ,  $Da = 10^{-6}$ ,  $\epsilon = 0.629$ , and  $c_F = 0.286$ . Finally, Case 3 is that modelled by Ledda *et al.* [27]: a slender plate normal to the flow with  $\chi = 10$ , where  $Re = 30$ ,  $Da = 1.1 \times 10^{-3}$ ,  $\epsilon = 0.650$ , and  $c_F = 0$ . For these three cases, we consider the errors in the estimates of  $C_D$ , the  $X$ -coordinate of the downstream saddle point S2, denoted by  $X_{S2}$ , and the Strouhal number  $St$ . We follow the verification and validation procedure outlined in Viola *et al.* [42]. This method was originally developed for yacht sails and was successively adopted for a wide range of applications, including the flow past the pappus of the dandelion diaspore [43], permeable disks [33], oscillating flapping foils [44], wind turbines [45], tidal turbines [46], arrays of energy harvesters [47], and ship hulls [48].

We consider four domains and three grids. The domains are built by progressively extending  $L_u$  and  $L_d$  by steps of 5 and 20, respectively. Specifically,  $L_u = 10, 15, 20, 25$  and  $L_d = 40, 60, 80, 100$  for domain D1 to D4, respectively. The grid spacing is the same for all domains, while the total number of grid points increases from D1 to D4. The G2 and G3 grids are achieved by scaling each cell size of G1 by  $\sqrt{2}$  and 2, respectively. Hence, the number of grid points along the domain boundaries is  $n_X = 350,492,700; n_Y = 210,295,420$ ; and along the width and thickness of the plate is  $n_d = n_t = 60,84,120$  for G1 to G3, respectively. The base grid G2 is used for the domain size investigation, and the base domain D3 is used for the grid resolution investigation.

We consider the relative change ( $\phi$ ) of a generic scalar with respect to the value computed with the base setting, with the relative change ( $h$ ) of a source of error. The latter is chosen such that  $h \rightarrow 0$  when the source of error vanishes. For example, Figure 2a shows the relative change of the drag coefficient,  $\phi_{C_D} = C_D/C_{D_{\text{base}}}$ , with the inverse of the relative domain size,  $h = h_d = (L_u/L_{u_{\text{base}}})^{-1} = 20/L_u$ . Figure 2b shows the relative change of S2's X-coordinate,  $\phi_{X_{S2}} = X_{S2}/X_{S2_{\text{base}}}$ , with the inverse of the relative number of cells,  $h = h_g = (n_X/n_{X_{\text{base}}})^{-1} = 492/n_X$ .

We fit the data with  $\phi = ch^p + \phi_0$ , where the coefficients  $c$ ,  $p$  and  $\phi_0$  are computed with least square optimisation, and the standard deviation of the residuals is  $\sigma$ . The advantage of presenting the data in this form is that the extrapolated value  $\phi_0$  for  $h \rightarrow 0$  is the expected true value of  $\phi$ . For example, in Figure 2a and 2b, the extrapolated values  $\phi_0$  are ca. 0.96 and 1.005, which is about 4% lower and 0.05% higher than those computed with the base domain and grid. Hence, these latter values computed as  $\delta = 1 - \phi_0$ , are the estimated errors. This procedure is used for both the modelling error due to the domain size, and the numerical error due to the grid size. Table I shows the modelling errors  $\delta_{C_D}$ ,  $\delta_{X_{S2}}$ , and  $\delta_{St}$  in the computation of  $C_D$ ,  $X_{S2}$  and  $St$ , respectively, for Case 1 and Case 2.

For the numerical error due to the grid resolution, we compute the 95% confidence interval  $[-U_{\phi}, U_{\phi}]$  centred on the value computed with the base setting (G2). The uncertainty  $U_{\phi}$  is computed differently depending on the order of convergence  $p$  of the least square fit. Specifically, for  $p \geq 0.95$ ,  $U_{\phi} = 1.25|\delta_{\phi}| + \sigma$ . For  $p < 0.95$ ,  $U_{\phi} = 1.5\Delta_{\phi} + \sigma$ , where  $\Delta_{\phi} = [\max(\phi) - \min(\phi)]/[1 - \min(h)/\max(h)]$ . This estimate is valid for any  $p < 0.95$ , but when  $-0.05 \leq p \leq 0.05$ , the confidence interval can alternatively be centred on the mean of all the computed values, and the uncertainty estimated as  $U_{\phi_{\text{mean}}} = 2(\sigma_{\phi}/\sqrt{N})$ , where  $N$  is the number of step sizes used and  $\sigma_{\phi}$  is the standard deviation of the distribution of  $\phi$ . Here, we adopt this second approach for  $St$ . Table II shows the uncertainty in the computation of  $C_D$ ,  $X_{S2}$  and  $St$  for Case 1 and Case 2. The values of the  $p$  coefficient for the cases shown in table II are as follows. Case 1:  $p_{C_D} = 0.57$ ,  $p_{X_{S2}} = 1.56$ . Case 2:  $p_{C_D} = 0.02$ ,  $p_{St} = 0.05$ .

TABLE I: Modelling error due to the finite domain size for  $C_D$ ,  $X_{S2}$  and  $St$  for a porous square cylinder. Case 1:  $\chi = 1, Re = 30, Da = 10^{-3}, \epsilon = 0.977, c_F = 0.148$  (steady); Case 2:  $\chi = 1, Re = 75, Da = 10^{-6}, \epsilon = 0.629, c_F = 0.286$  (unsteady).

Domain	$h_d$	$C_D$	Case 1			Case 2		
			$\delta_{C_D}(\%)$	$X_{S2}$	$\delta_{X_{S2}}(\%)$	$C_D$	$\delta_{C_D}(\%)$	$St$
D1	0.50	1.9444	8.76	1.9455	1.01	1.5244	6.14	0.1366
D2	0.75	1.8763	5.07	1.9431	0.89	1.4834	3.34	0.1337
D3	1.00	1.8463	3.45	1.9371	0.58	1.4664	2.18	0.1324
D4	1.25	1.8297	2.55	1.9321	0.32	1.4572	1.55	0.1318

TABLE II: Uncertainty due to finite grid resolution for  $C_D$ ,  $X_{S2}$  and  $St$  for a porous square cylinder. Case 1:  $\chi = 1, Re = 30, Da = 10^{-3}, \epsilon = 0.977, c_F = 0.148$  (steady); Case 2:  $\chi = 1, Re = 75, Da = 10^{-6}, \epsilon = 0.629, c_F = 0.286$  (unsteady).

Grid	$h_g$	Case 1		Case 2	
		$C_D, U_{C_D}(\%)$	$X_{S2}, U_{X_{S2}}(\%)$	$C_D, U_{C_D}(\%)$	$St, U_{St}(\%)$
G1	$\sqrt{2}$	1.8306, 4.65	1.9292, 1.22	1.4637, 0.21	0.1331, 1.27
G2	1	1.8463, 4.65	1.9371, 0.71	1.4664, 0.21	0.1324, 1.27
G3	$1/\sqrt{2}$	1.8592, 4.65	1.9417, 0.41	1.4609, 0.21	0.1303, 1.27

The values of  $C_D$ ,  $X_{S2}$  and  $St$  computed with the base setting (D3, G2) are compared with those of other authors in table III. The differences are consistent with the modelling errors due to the finite domain size and the numerical uncertainty. Note that Dhinakaran and Ponmozhi [25] and Anirudh and Dhinakaran [26] have used domains that are about half of D3 in size, and this is consistent with their higher estimates of  $C_D$ ,  $X_{S2}$  and  $St$ .

Overall, the numerical and modelling error analysis reveals that the estimate of the forces and of the coordinates of topological

points in the wake are predicted within a numerical uncertainty at a 95% confidence level of 4.65% and 0.71%, respectively. The error due to the finite size of the domain is estimated at 5.07% and 0.89%, respectively.

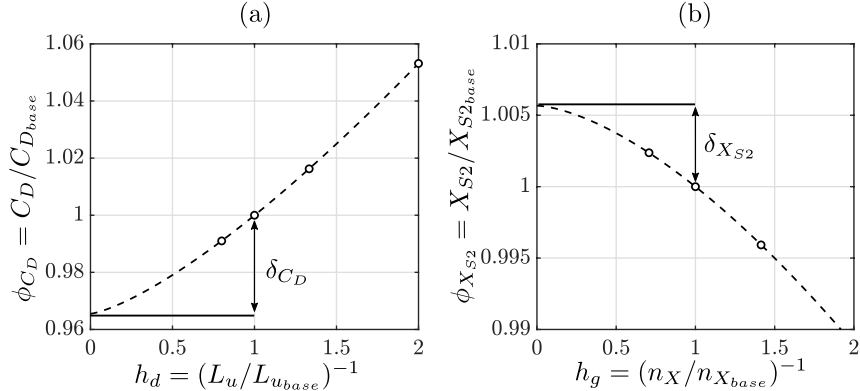


FIG. 2: Convergence of the drag coefficient with the domain size (a) and of the  $X$ -coordinate of the downstream saddle point with the grid resolution (b) for Case I.

TABLE III: Present study results compared with three cases from the literature. Case 1:

$\chi = 1, Re = 30, Da = 10^{-3}, \epsilon = 0.977, c_F = 0.148$  (steady); Case 2:  $\chi = 1, Re = 75, Da = 10^{-6}, \epsilon = 0.629, c_F = 0.286$  (unsteady); Case 3:  $\chi = 4, Re = 30, Da = 1.1 \times 10^{-3}, \epsilon = 0.650, c_F = 0.0$ .

	Case 1	Case 2	Case 3			
	$C_D$	$X_{S2}$	$C_D$	$St$	$C_D$	$X_{S2}$
Anirudh and Dhinakaran (2018)	2.0021	1.9820	1.5639	0.1374	-	-
Dhinakaran and Ponmozhi (2011)	2.0255	1.9415	-	-	-	-
Sharma and Eswaran (2004)	-	-	1.5490	0.1370	-	-
Ledda et al. (2018)	-	-	-	-	1.86	2.15
Present study	1.8463	1.9371	1.4664	0.1324	1.77	2.07

### III. RESULTS AND DISCUSSIONS

#### A. Steady-unsteady transition boundary

First, we investigate the  $Re$  and  $Da$  values for which the wake is steady and unsteady for flow incidences  $\alpha = 40^\circ$  and  $90^\circ$  (figs. 3a and 3b, respectively). At both incidences, the critical  $Re$  value at which steady-unsteady transition occurs increases with  $Da$ , and decreases with  $\alpha$  (solid line in figs. 3a and 3b). We also identify the transition between a steady wake with and without a recirculation region (dashed line in figs. 3a and 3b). At  $\alpha = 90^\circ$ , this transition occurs at  $3 \times 10^{-4} < Da < 5 \times 10^{-4}$ , and it seems independent of  $Re$ . Instead, at  $\alpha = 40^\circ$ , the critical  $Da$  at which this transition occurs decreases with  $Re$ . Finally, we observe that at  $\alpha = 40^\circ$ , wake patterns exist with either one or two recirculation regions, whereas the single recirculation region exists only at low  $Re$  and  $Da$  values. At  $Re = 30$ , the wake is always steady for any value of  $Da$  and  $\alpha$ , and might present two, one, or no recirculation regions depending on  $Da$  and  $\alpha$ . In the rest of the paper, we investigate how the permeability allows switching between these three different flow topologies, and we focus on  $Re = 30$  to ensure that the wake remains steady.

#### B. Porous plate normal to the stream

We first consider a plate at  $Re = 30$  and  $\alpha = 90^\circ$ , where two recirculation regions are formed as shown in Fig.1b, and we investigate the effect of permeability. Figure 4a shows the  $X$  coordinate of the upstream (S1) and downstream (S2) saddle points versus  $Da$ , while Fig. 4b shows  $C_D$  versus  $Da$ . For vanishing permeability ( $Da \rightarrow 0$ ), the flow topology and the force tend

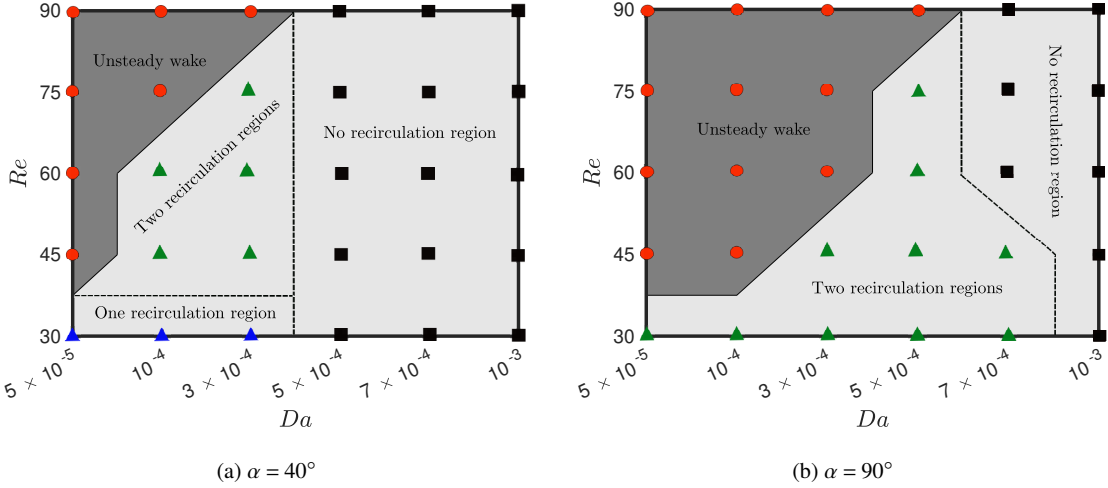


FIG. 3: Map of the wake topology for a 2D porous plate for a range of Reynolds and Darcy numbers. The light grey region and the deep grey region represent the steady and unsteady wake regions, respectively. The red circles, blue and green triangles, and black squares are indicative of unsteady vortex shedding, one and two recirculation regions, and no recirculation, respectively.

asymptotically towards those of an impervious plate. The small differences between the results for an impervious plate and the asymptotic values for vanishing  $Da$  are attributed to the different numerical algorithms for porous and impervious bodies. As  $Da$  increases, S1 moves downstream, and S2 moves upstream, shrinking the vortex dipole up to its annihilation at a critical  $Da$ , between  $8 \times 10^{-4}$  and  $9 \times 10^{-4}$ . This is also shown in figs. 4c-4e by means of the streamlines superimposed to the vorticity contour. The reduction in size and eventual annihilation of the vortex dipole coincides with a reduction in  $C_D$ . The  $C_D$  values obtained for an axisymmetric porous disc by Cummins *et al.* [33] at  $Re = 30$  are relatively higher than those obtained for a 2D flat plate in this study. However, the trend of  $C_D$  variation with respect to  $Da$  is qualitatively similar in these two cases.

### C. Flow around a porous plate at incidence

We now turn our study to the effect of the angle of incidence on permeable plates. With decreasing  $\alpha$  from  $90^\circ$  to  $0^\circ$ , the vortex dipole first becomes asymmetric and eventually annihilates. This occurs through different topological steps for low and high permeability values. For plates with low permeability, as well as for the impervious plates, the recirculating wake annihilates in two steps as  $\alpha$  is decreased. Conversely, beyond a critical  $Da$  value, between  $5 \times 10^{-5}$  and  $5 \times 10^{-4}$ , the vortex dipole annihilates in a single step. This is shown in figs. 5a and 5b for low and high permeability cases ( $Da = 5 \times 10^{-5}$  and  $5 \times 10^{-4}$ ), respectively, where the body-fixed coordinates of the topological points (N1, N2, S1, and S2) are tracked for various incidences.

For the low-permeability case, with decreasing  $\alpha$ , all four topological points move first downstream parallel with  $y$  and then turn towards the plate (Fig. 5c). At  $\alpha = 44^\circ$ , N2 merges with S2, forming a distinct topological field, comprising only one re-circulation region with closed streamlines and negative circulation (Fig. 5d). This topology exists for  $\alpha$  as low as  $30^\circ$ , when N1 merges with S1 annihilating the re-circulation region (Fig. 5e). In contrast, for the high-permeability case, the intermediate topology with only one re-circulation region does not exist (Fig. 5f). Instead, both node-saddle point pairs merge at  $\alpha = 64^\circ$  (Fig. 5g). For lower values of  $\alpha$ , the wake is characterised by tortuous streamlines with no closed re-circulation regions (Fig. 5h).

### D. Forces and torque on a porous plate at incidence

Akin to the porous plate normal to the stream, both  $C_L$  and  $C_D$  decrease with increasing permeability at any  $\alpha$  (Fig. 6a and 6b). The lift and the torque vanish at  $\alpha = 0^\circ$  and  $90^\circ$ , and their absolute value is maximum for the same critical incidence,  $\alpha_{\max}$ , which increases with the permeability. Interestingly, at  $Da = 5 \times 10^{-5}$ ,  $C_L$  and  $|C_M|$  are maximum at  $\alpha = 34^\circ$ , where the wake is characterised by a single clockwise recirculation region; while at  $Da = 10^{-3}$ ,  $C_L$  and  $|C_M|$  are maximum near  $\alpha = 40^\circ$ , where there is no recirculation region. The  $C_D$  value, which increases monotonically from  $\alpha = 0^\circ$  to  $90^\circ$ , shows a higher reduction with permeability at  $\alpha = 90^\circ$  than  $0^\circ$ .

In the body-fixed frame of reference, while  $C_x$  decreases with  $Da$  (Fig. 6c),  $|C_y|$  increases with  $Da$  for any  $\alpha$  between  $20^\circ$  and

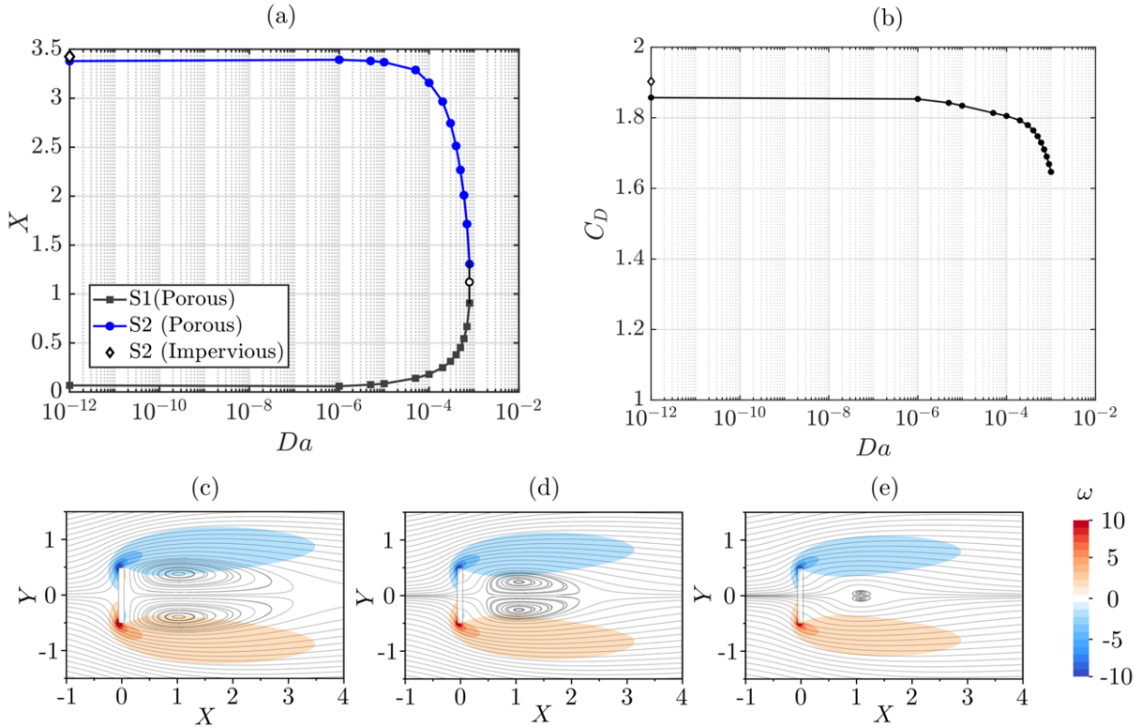


FIG. 4: (a) Stream-wise coordinate of saddle points S1 and S2, and (b) drag coefficient versus the Darcy number for a 2D porous plate with  $\alpha = 90^\circ$  and  $Re = 30$ , where diamonds indicate the values for a solid plate at the same  $\alpha$  and  $Re$ . Streamlines and vorticity field,  $\omega$ , for (c)  $Da = 5 \times 10^{-5}$ , (d)  $Da = 5 \times 10^{-4}$ , and (e)  $Da = 8 \times 10^{-4}$ .

$90^\circ$ ; see figs. 6d and 6e. To understand this result, we estimate the force components in the four faces of the porous plate, F1-F4, as defined in the inset of Fig. 6. For each face, we consider the pressure and viscous components of  $C_x$  and  $C_y$ . The plate-normal force coefficient  $C_x$  is primarily driven by the suction on F2 and, to a lesser extent, by the pressure on F4 (Fig. 6f). This is akin to a foil at incidence. Both the force contributions decrease with permeability, as expected. In contrast,  $C_y$  is primarily driven by the shear on F4 and to a lesser extent, by the suction on F3 (Fig. 6g). The increase in shear on F4 with increasing  $Da$  is primarily responsible for the overall increase in  $C_y$  (Fig. 6d).

#### E. Force calculation from the fluid impulse

We aim to investigate how the vorticity field around the plate varies with the permeability, and how these changes are correlated with the forces. For steady 2D flows, the relationship between the vorticity field and the lift is given by the Kutta-Joukowsky lift formula, which, in nondimensional form, is  $L = -\Gamma$ , where  $\Gamma$  is the nondimensional circulation and  $C_L = 2L$ . For steady flow conditions,  $\Gamma$  should be computed as the integral of vorticity over a region enclosing the plate, such that the net flux of vorticity across the region boundary vanishes [49]. Here, we consider the integral of vorticity within the whole domain.

For steady 2D flows, the non-dimensional drag  $D$  is [49]

$$D = - \int_W Y \omega \, dW, \quad (4)$$

where the line  $W$  orthogonally intersects the far wake, and  $C_D = 2D$ . Here, we chose  $W$  as a stream-normal section of the domain at  $X = 70$ . The comparison between the force coefficients computed with the impulse theory and with the stress tensor (eq. 3) is shown in Fig. 7.

From the Kutta-Joukowsky lift formula ( $L = -\Gamma$ ), we infer that the difference in the lift of two plates with different  $Da$  is proportional to the change in the integral of vorticity in the whole field. To gain insights into the underlying mechanism that leads to a lift change, we set out to investigate which region experiences the greatest change in vorticity due to a change in permeability. We consider the plate at  $\alpha = 40^\circ$  and three  $Da$  values: a low permeability case with  $Da = 5 \times 10^{-5}$ , where a single

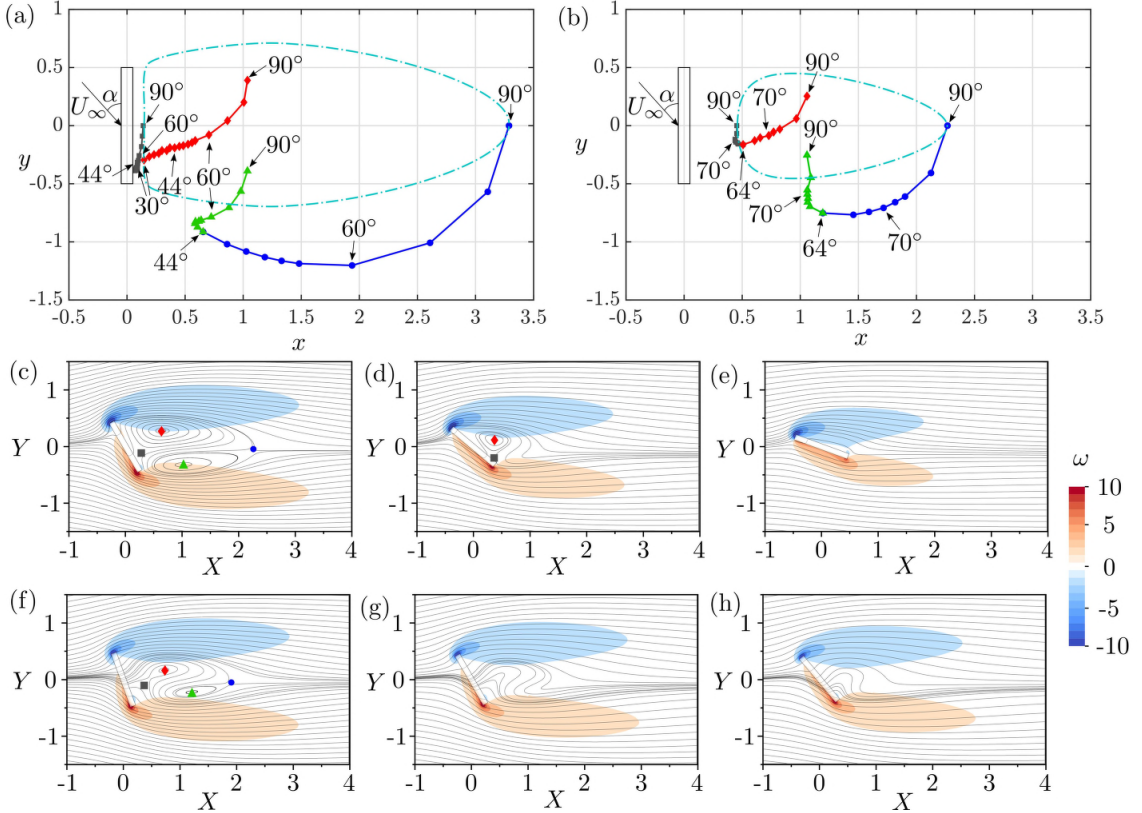


FIG. 5: Position of nodes N1 (red diamond), N2 (green triangle), and saddle points S1 (grey square), S2 (blue circle) of a 2D porous plate at  $Re = 30$  for (a)  $Da = 5 \times 10^{-5}$  and (b)  $Da = 5 \times 10^{-4}$ , where  $\alpha = [90^\circ, 80^\circ, 70^\circ, 60^\circ, 54^\circ, 52^\circ, 50^\circ, 48^\circ, 46^\circ, 44^\circ, 42^\circ, 40^\circ, 38^\circ, 36^\circ, 34^\circ, 32^\circ, 30^\circ]$  in (a),  $\alpha = [90^\circ, 80^\circ, 74^\circ, 72^\circ, 70^\circ, 68^\circ, 66^\circ, 64^\circ]$  in (b), and light blue dotted lines denote the closed streamline of the vortex dipole at  $\alpha = 90^\circ$ . Streamlines and vorticity field for  $Da = 5 \times 10^{-5}$  and (c)  $\alpha = 60^\circ$ , (d)  $\alpha = 40^\circ$ , and (e)  $\alpha = 20^\circ$ . Streamlines and vorticity field for  $Da = 5 \times 10^{-4}$  and (f)  $\alpha = 70^\circ$ , (g)  $\alpha = 60^\circ$ , and (h)  $\alpha = 50^\circ$ . When present, the positions of N1, N2, S1, and S2 are indicated.

recirculation zone with negative circulation exists (Fig. 5d); a high permeability case with  $Da = 5 \times 10^{-4}$ , where there are no close recirculation regions (Fig. 5g); and the maximum permeability case, investigated in this study, with  $Da = 10^{-3}$ . Here, the terms ‘low-permeability’ and ‘high-permeability’ are used consistently with the previous sections. The vorticity fields of the low, high, and max permeability cases are denoted as  $\omega_L$ ,  $\omega_H$ , and  $\omega_M$ , respectively. The lift and drag coefficients for these three cases are shown in table IV.

TABLE IV: Lift and drag coefficients computed with the stress tensor and with impulse theory for  $\alpha = 40^\circ$  and three values of the Darcy number

	$Da = 5 \times 10^{-5}$		$Da = 5 \times 10^{-4}$		$Da = 10^{-3}$	
	$C_L$	$C_D$	$C_L$	$C_D$	$C_L$	$C_D$
Conventional	0.960	1.280	0.751	1.228	0.594	1.142
Impulse Theory	1.021	1.292	0.781	1.237	0.586	1.174

The spatial distributions of the differential vorticity fields  $\omega_H - \omega_L$  and  $\omega_M - \omega_H$  (figs. 8a and 8b, respectively) show how each fluid region contribute to the change in the lift. Four distinct regions are observed: two associated with the leading and trailing edge shear layers, and two associated with the suction and pressure side of the plate. For example, in Fig. 8, the threshold value of  $|\omega_t| = 0.48$  is used to clearly identify the four regions. The vorticity within each region is integrated to compute the

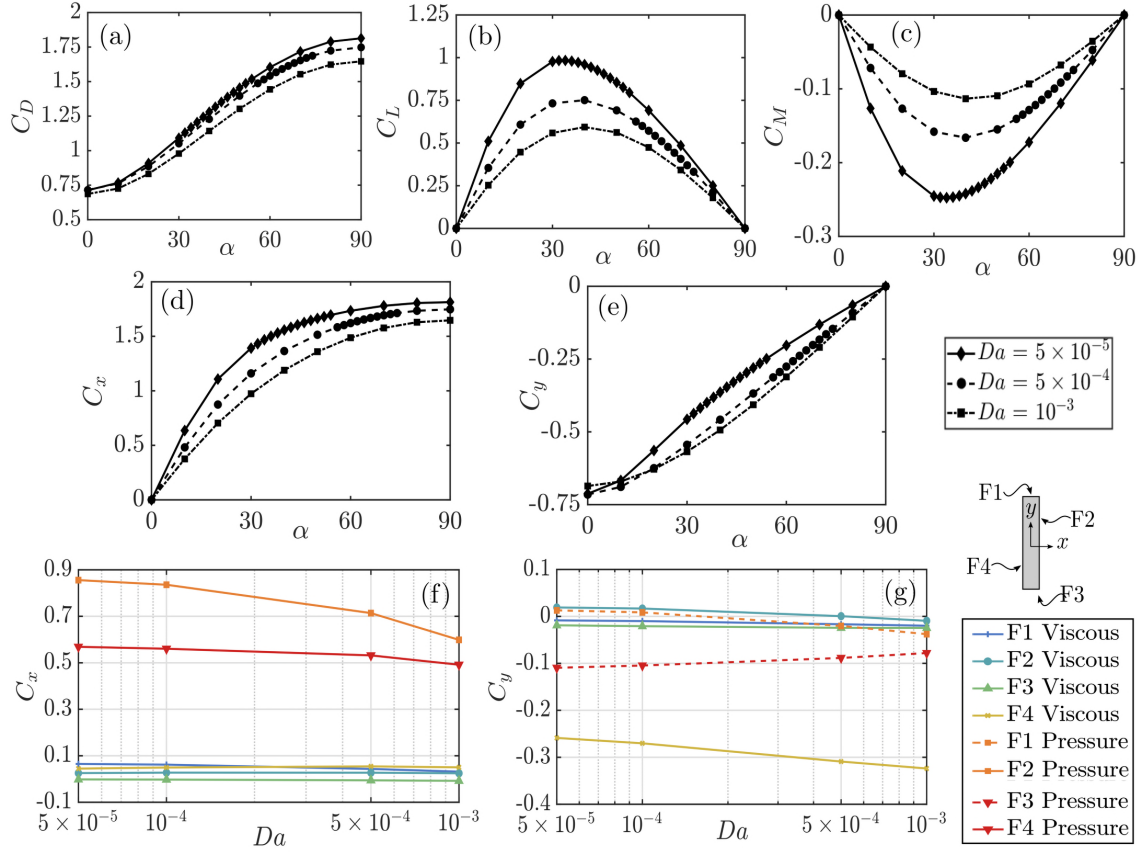


FIG. 6: Coefficients of (a) drag, (b) lift (c) torque, (d) plate-normal force (e) plate-wise force for porous plates with three different permeability values versus the flow incidence. (f) Plate-normal and (g) plate-wise pressure and viscous force coefficients for each face (F1, F2, F3 and F4) of a porous plate at  $\alpha = 40^\circ$  versus the Darcy number.

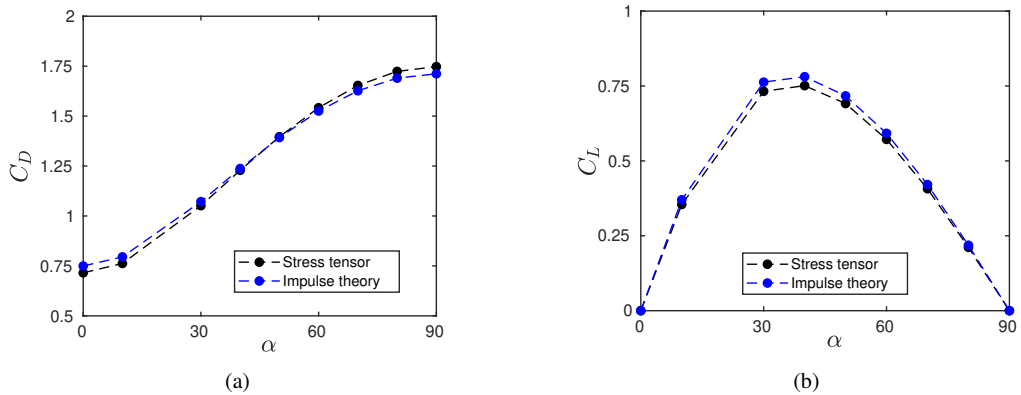


FIG. 7: Lift and drag coefficients are computed with the stress tensor and with impulse theory for different incidences at  $Da = 5 \times 10^{-4}$ .

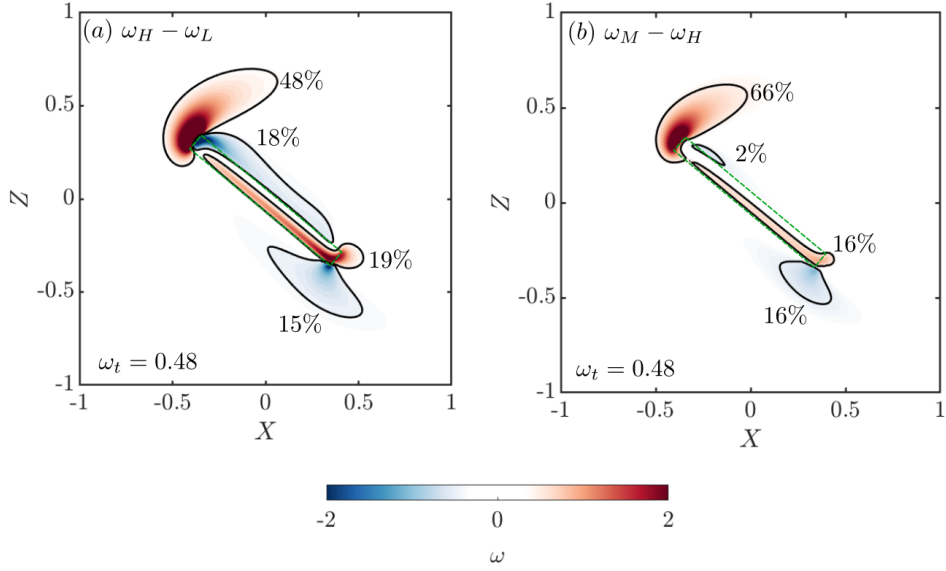


FIG. 8: Differential vorticity fields for the porous plate at  $\alpha = 40^\circ$ : (a)  $\omega_H - \omega_L$ , and (b)  $\omega_M - \omega_H$ . The percentage values show the relative circulation of the four regions identified by the isolines of differential vorticity  $|\omega| = 0.48$ .

contribution to the total change in circulation, and thus, in lift. The percentage values indicate the absolute circulation fraction of each region over the summation of the absolute circulation of all four regions. It is noted that these percentage values are about independent of the threshold value  $\omega_t$ . For both  $\omega_H - \omega_L$  and  $\omega_M - \omega_H$ , the integral of the change of vorticity near the leading-edge is substantially higher than the change of vorticity in the other three marked flow regions. Hence, we conclude that the change in the strength of the leading edge shear layer is the main driver for the lift change. Furthermore, its dominant role compared to that of the two shear layers along the chord and that of the trailing edge shear layer increases with  $Da$  (e.g. from 48% to 66% in Fig. 8).

To investigate how changes in the vorticity field due to the increased permeability are correlated with the loss of drag, we consider the first moment of vorticity in the stream-wise direction,  $Y\omega$ , whose integral along the line  $W$  is the drag (eq. 4). The leading- and trailing-edge vortex sheet results in two peaks (Fig. 9a), whose amplitude decreases with permeability, while their width is constant. This result suggests that the drop in drag with an increased permeability is primarily due to the weakening of the strength of the vortex sheet and not, for example, by the reduction of the width of the wake. To quantify the relative effect of the leading- and trailing-edge vortex sheet strength on the change of drag coefficient, we consider the difference of the first moment of vorticity in the stream-wise direction for the  $\omega_L - \omega_H$  and  $\omega_H - \omega_M$  cases; see Fig. 9b. The figure also shows the zeros of the functions  $Y|\Delta\omega| = 0$  for  $\Delta\omega = \omega_L - \omega_H$  ( $A_1 - D_1$ ), and for  $\Delta\omega = \omega_H - \omega_M$  ( $A_2 - D_2$ ). By computing the integral along  $Y$  between consecutive zeros, we find that for the  $\omega_L - \omega_H$  case, the changes in  $C_D$  due to the weakening of the leading- and trailing-edge vortex sheet are 0.0251 and 0.0555, respectively; whereas, the corresponding changes in  $C_D$  for the ( $\omega_H - \omega_M$ ) case are 0.0192 and 0.0577, respectively. These results suggest that, with the increased permeability, the weakening of the trailing-edge vortex sheet is more significant than that of the leading-edge vortex sheet on the drag reduction.

#### IV. CONCLUSIONS

The flow behind a 2D porous plate is investigated for different values of the permeability ( $Da$ ) and flow incidence ( $\alpha$ ). The flow typology is investigated for Reynolds number ( $Re$ ) values between 30 and 90, while a detailed analysis of the forces is undertaken at  $Re = 30$ , where the wake is found to be steady for any  $Da$  and  $\alpha$ . An incompressible Navier-Stokes solver of the open-source library OpenFOAM has been modified to solve for the Darcy-Brinkman-Forchheimer equation in the porous region.

For a porous plate normal to the stream, below a critical Darcy number, between  $8 \times 10^{-4}$  and  $9 \times 10^{-4}$ , a vortex dipole with two saddles and two nodes is formed in the wake. With increasing  $Da$ , the separation of the dipole from the plate increases and both the pairs of topological points merge, eventually annihilating the dipole.

With decreasing  $\alpha$  from  $90^\circ$  to  $0^\circ$ , the vortex dipole annihilation process is distinct for low and high permeability cases

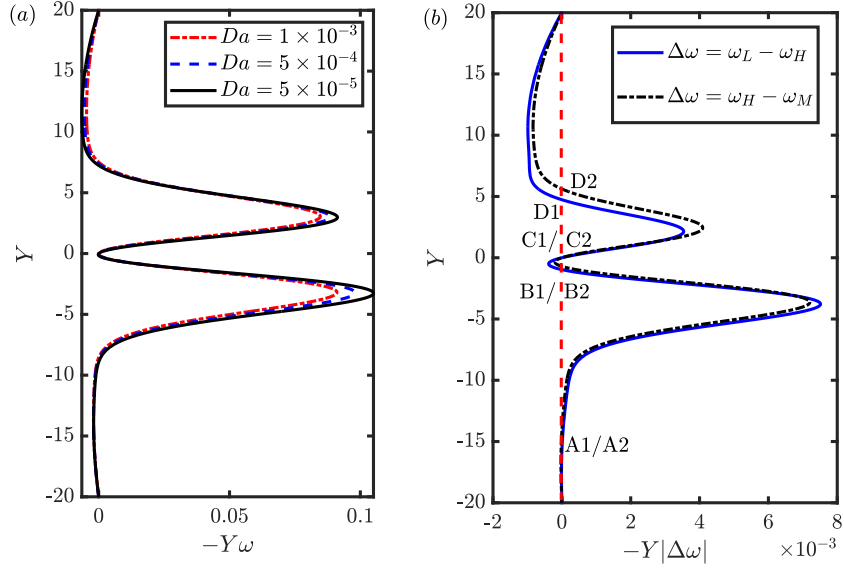


FIG. 9: (a) Stream-wise component of the negative first moment of the vorticity field  $-Y\omega$  and (b) the difference of the negative first moment of the vorticity field  $-Y|\Delta\omega|$  for the  $\omega_L - \omega_H$  and  $\omega_H - \omega_M$  cases along the  $X = 70$  line for  $\alpha = 40^\circ$  and  $Da = 5 \times 10^{-5}, 5 \times 10^{-4}$  and  $10^{-3}$ .

( $Da = 5 \times 10^{-5}$  and  $Da = 5 \times 10^{-4}$ ). For the former, first, the downstream saddle and node merge, forming a single recirculating region with negative circulation. With decreasing  $\alpha$  further, the upstream node and saddle merge, annihilating the recirculating region. Conversely, the four topological points for highly permeable plates merge at the same critical incidence. Lift, drag, and torque decrease in magnitude with  $Da$ , but there exists a range of  $\alpha$  and  $Da$  where the plate-wise force component increases in magnitude because of the shear force on the pressure side of the plate.

The steady and unsteady transition boundaries are compared for a representative value of  $\alpha = 40^\circ$  and the stream-normal condition. It is observed that the wake remains steady for higher  $Re$  and lower  $Da$  values when the porous plate is at an incidence as compared to the stream-normal condition.

The analysis of the rate of change of the flow impulse suggests that effect of an increased permeability is to decrease the lift by weakening the leading-edge shear layer, and to decrease the drag by weakening the trailing edge shear layer.

## V. ACKNOWLEDGEMENTS

This work was funded by the ERC Consolidator Grant ‘Dandidrone’ (101001499), and Callum Bruce’s scholarship was funded by the EPSRC grant EP/S023801/1.

## DATA AVAILABILITY STATEMENT

The data that support the findings of this study are available from the first author/corresponding author upon reasonable request.

#### DECLARATION OF INTERESTS

The authors report no conflict of interest.

---

- [1] H. Klippstein, H. Hassanin, A. Diaz De Cerio Sanchez, Y. Zweiri, and L. Seneviratne, Additive manufacturing of porous structures for unmanned aerial vehicles applications, *Advanced Engineering Materials* **20**, 1800290 (2018).
- [2] V. Selivanov, M. Silnikov, V. Markov, Y. V. Popov, and V. Pusev, Using highly porous aluminum alloys and honeycomb structures in spacecraft landing gear, *Acta Astronautica* **180**, 105 (2021).
- [3] K. A. Moore, Influence of seagrasses on water quality in shallow regions of the lower chesapeake bay, *Journal of Coastal Research* , 162 (2009).
- [4] Z. Chen, A. Ortiz, L. Zong, and H. Nepf, The wake structure behind a porous obstruction and its implications for deposition near a finite patch of emergent vegetation, *Water Resources Research* **48** (2012).
- [5] F. Wen, D.-S. Jeng, J. Wang, and X. Zhou, Numerical modeling of response of a saturated porous seabed around an offshore pipeline considering non-linear wave and current interaction, *Applied Ocean Research* **35**, 25 (2012).
- [6] C. Cummins, M. Seale, A. Macente, D. Certini, E. Mastropaolo, I. M. Viola, and N. Nakayama, A separated vortex ring underlies the flight of the dandelion, *Nature* **562**, 414 (2018).
- [7] V. Iyer, H. Gaensbauer, T. L. Daniel, and S. Gollakota, Wind dispersal of battery-free wireless devices, *Nature* **603**, 427 (2022).
- [8] A. Fage and F. Johansen, On the flow of air behind an inclined flat plate of infinite span, *Proceedings of the Royal Society of London, Series A* **116**, 170 (1927).
- [9] D. Ingham, T. Tang, and B. Morton, Steady two-dimensional flow through a row of normal flat plates, *Journal of Fluid Mechanics* **210**, 281 (1990).
- [10] S. Dennis, W. Qiang, M. Coutanceau, and J.-L. Launay, Viscous flow normal to a flat plate at moderate reynolds numbers, *Journal of Fluid Mechanics* **248**, 605 (1993).
- [11] K. Lam and M. Y. Leung, Asymmetric vortex shedding flow past an inclined flat plate at high incidence, *European Journal of Mechanics-B/Fluids* **24**, 33 (2005).
- [12] S. Wu, J.-J. MIAU, C. Hu, and J. Chou, On low-frequency modulations and three-dimensionality in vortex shedding behind a normal plate, *Journal of Fluid Mechanics* **526**, 117 (2005).
- [13] S. Taneda, Standing twin-vortices behind a thin flat plate normal to the flow(standing twin vortices in wake behind thin flat plate normal to flow visualized by al dust, noting karman vortex street), *Kyushu University, Research Institute for Applied Mechanics Reports* **16**, 155 (1968).
- [14] J. Hudson and S. Dennis, The flow of a viscous incompressible fluid past a normal flat plate at low and intermediate reynolds numbers: the wake, *Journal of Fluid Mechanics* **160**, 369 (1985).
- [15] K. In, D. H. Choi, and M. Kim, Two-dimensional viscous flow past a flat plate, *Fluid Dynamics Research* **15**, 13 (1995).
- [16] A. K. Saha, Far-wake characteristics of two-dimensional flow past a normal flat plate, *Physics of Fluids* **19**, 128110 (2007).
- [17] J. Zhang, N.-S. Liu, and X.-Y. Lu, Route to a chaotic state in fluid flow past an inclined flat plate, *Physical Review E* **79**, 045306 (2009).
- [18] A. K. Saha, Direct numerical simulation of two-dimensional flow past a normal flat plate, *Journal of Engineering Mechanics* **139**, 1894 (2013).
- [19] A. Hemmati, D. H. Wood, and R. J. Martinuzzi, On simulating the flow past a normal thin flat plate, *Journal of Wind Engineering and Industrial Aerodynamics* **174**, 170 (2018).
- [20] T. Miyagi, Standing vortex-pair behind a flat plate normal to uniform flow of viscous fluid, *Journal of the Physical Society of Japan* **45**, 1751 (1978).
- [21] A. Mashhadi, A. Sohankar, and M. M. Alam, Flow over rectangular cylinder: Effects of cylinder aspect ratio and reynolds number, *International Journal of Mechanical Sciences* **195**, 106264 (2021).
- [22] M. Rastan, M. M. Alam, H. Zhu, and C. Ji, Onset of vortex shedding from a bluff body modified from square cylinder to normal flat plate, *Ocean Engineering* **244**, 110393 (2022).
- [23] I. Tani, Low-speed flows involving bubble separations, *Progress in Aerospace Sciences* **5**, 70 (1964).
- [24] J. A. Smith, G. Pisetta, and I. M. Viola, The scales of the leading-edge separation bubble, *Physics of Fluids* **33**, 045101 (2021).
- [25] S. Dhinakaran and J. Ponmozhi, Heat transfer from a permeable square cylinder to a flowing fluid, *Energy Conversion and Management* **52**, 2170 (2011).
- [26] K. Anirudh and S. Dhinakaran, On the onset of vortex shedding past a two-dimensional porous square cylinder, *Journal of Wind Engineering and Industrial Aerodynamics* **179**, 200 (2018).
- [27] P. G. Ledda, L. Siconolfi, F. Viola, F. Gallaire, and S. Camarri, Suppression of von kármán vortex streets past porous rectangular cylinders, *Physical Review Fluids* **3**, 103901 (2018).
- [28] T. Tang, P. Yu, S. Yu, X. Shan, and H. Chen, Connection between pore-scale and macroscopic flow characteristics of recirculating wake behind a porous cylinder, *Physics of Fluids* **32**, 083606 (2020).
- [29] P. Yu, Y. Zeng, T. S. Lee, X. B. Chen, and H. T. Low, Steady flow around and through a permeable circular cylinder, *Computers & Fluids* **42**, 1 (2011).
- [30] P. J. Baddoo, R. Hajian, and J. W. Jaworski, Unsteady aerodynamics of porous aerofoils, *Journal of Fluid Mechanics* **913** (2021).
- [31] P. Yu, Y. Zeng, T. S. Lee, X. B. Chen, and H. T. Low, Numerical simulation on steady flow around and through a porous sphere, *International Journal of Heat and Fluid Flow* **36**, 142 (2012).

- [32] M. Ciuti, G. Zampogna, F. Gallaire, S. Camarri, and P. Ledda, On the effect of a penetrating recirculation region on the bifurcations of the flow past a permeable sphere, *Physics of Fluids* **33**, 124103 (2021).
- [33] C. Cummins, I. M. Viola, E. Mastropaoletti, and N. Nakayama, The effect of permeability on the flow past permeable disks at low reynolds numbers, *Physics of Fluids* **29**, 097103 (2017).
- [34] P. G. Ledda, L. Siconolfi, F. Viola, S. Camarri, and F. Gallaire, Flow dynamics of a dandelion pappus: A linear stability approach, *Physical Review Fluids* **4**, 071901 (2019).
- [35] T. Tang, J. Xie, S. Yu, J. Li, and P. Yu, Effect of aspect ratio on flow through and around a porous disk, *Phys. Rev. Fluids* **6**, 074101 (2021).
- [36] H. Darcy, *Les fontaines publiques de la ville de Dijon*, Vol. 2 (V. Dalmont, 1856).
- [37] H. C. Brinkman, A calculation of the viscous force exerted by a flowing fluid on a dense swarm of particles, *Flow, Turbulence and Combustion* **1**, 27 (1949).
- [38] I. Castro, Wake characteristics of two-dimensional perforated plates normal to an air-stream, *Journal of Fluid Mechanics* **46**, 599 (1971).
- [39] J. Graham, Turbulent flow past a porous plate, *Journal of Fluid Mechanics* **73**, 565 (1976).
- [40] M. Cicolini, S. Chellini, B. Usherwood, B. Ganapathisubramani, and I. P. Castro, Vortex shedding behind porous flat plates normal to the flow, *Journal of Fluid Mechanics* **985**, A40 (2024).
- [41] D. D. Joseph, D. A. Nield, and G. Papanicolaou, Nonlinear equation governing flow in a saturated porous medium, *Water Resources Research* **18**, 1049 (1982).
- [42] I. M. Viola, P. Bot, and M. Riotte, On the uncertainty of cfd in sail aerodynamics, *International Journal for Numerical Methods in Fluids* **72**, 1146 (2013).
- [43] C. Cummins, M. Seale, A. Macente, D. Certini, E. Mastropaoletti, I. M. Viola, and N. Nakayama, A separated vortex ring underlies the flight of the dandelion, *Nature* **562**, 414 (2018).
- [44] E. Wang, K. Ramesh, S. Killen, and I. M. Viola, On the nonlinear dynamics of self-sustained limit-cycle oscillations in a flapping-foil energy harvester, *Journal of Fluids and Structures* **83**, 339 (2018).
- [45] W. Dai, R. Broglia, and I. M. Viola, Mitigation of rotor thrust fluctuations through passive pitch, *Journal of Fluids and Structures* **112**, 103599 (2022).
- [46] B. Chen, S. Su, I. M. Viola, and C. A. Greated, Numerical investigation of vertical-axis tidal turbines with sinusoidal pitching blades, *Ocean Engineering* **155**, 75 (2018).
- [47] I. M. Viola, Z. Gao, and J. Smith, Use of streamnormal forces within an array of tidal power harvesters, *Plos One* **17**, e0270578 (2022).
- [48] N. Speranza, B. Kidd, M. P. Schultz, and I. M. Viola, Modelling of hull roughness, *Ocean Engineering* **174**, 31 (2019).
- [49] I. M. Viola, A. Arredondo-Galeana, and G. Pisetta, The force generation mechanism of lifting surfaces with flow separation, *Ocean Engineering* **239**, 109749 (2021).
- [50] A. Sharma and V. Eswaran, Heat and fluid flow across a square cylinder in the two-dimensional laminar flow regime, *Numerical Heat Transfer, Part A: Applications* **45**, 247 (2004).
- [51] M. Shademan and A. Naghib-Lahouti, Effects of aspect ratio and inclination angle on aerodynamic loads of a flat plate, *Advances in Aerodynamics* **2**, 1 (2020).
- [52] K. R. Raju, R. Garde, S. Singh, and N. Singh, Experimental study on characteristics of flow past porous fences, *Journal of Wind Engineering and Industrial Aerodynamics* **29**, 155 (1988).
- [53] F.-M. Fang and D. Wang, On the flow around a vertical porous fence, *Journal of wind engineering and industrial aerodynamics* **67**, 415 (1997).
- [54] K. Steiros and M. Hultmark, Drag on flat plates of arbitrary porosity, *Journal of Fluid Mechanics* **853** (2018).
- [55] C.-T. Hsu and P. Cheng, Thermal dispersion in a porous medium, *International Journal of Heat and Mass Transfer* **33**, 1587 (1990).
- [56] G. Neale and W. Nader, Practical significance of brinkman's extension of darcy's law: coupled parallel flows within a channel and a bounding porous medium, *The Canadian Journal of Chemical Engineering* **52**, 475 (1974).
- [57] K. Vafai and S. Kim, On the limitations of the brinkman-forchheimer-extended darcy equation, *International Journal of Heat and Fluid Flow* **16**, 11 (1995).
- [58] J. A. Ochoa-Tapia and S. Whitaker, Momentum transfer at the boundary between a porous medium and a homogeneous fluid—i. theoretical development, *International Journal of Heat and Mass Transfer* **38**, 2635 (1995).
- [59] D. Nield, The limitations of the brinkman-forchheimer equation in modeling flow in a saturated porous medium and at an interface, *International Journal of Heat and Fluid Flow* **12**, 269 (1991).
- [60] G. S. Beavers and D. D. Joseph, Boundary conditions at a naturally permeable wall, *Journal of Fluid Mechanics* **30**, 197 (1967).